

Charge-transfer satellites and chemical bonding in photoemission and x-ray absorption of SrTiO₃ and rutile TiO₂: Experiment and first-principles theory with general application to spectroscopic analysis

J. C. Woicik,¹ C. Weiland,¹ C. Jaye,¹ D. A. Fischer,¹ A. K. Rumaiz,² E. L. Shirley,³ J. J. Kas,⁴ and J. J. Rehr⁴

¹*Materials Measurement Science Division, Material Measurement Laboratory, National Institute of Standards and Technology, Gaithersburg, Maryland 20899, USA*

²*National Synchrotron Light Source II, Brookhaven National Laboratory, Upton, New York 11973, USA*

³*Sensor Science Division, Physical Measurement Laboratory, National Institute of Standards and Technology, Gaithersburg, Maryland 20899, USA*

⁴*Department of Physics, University of Washington, Seattle, Washington 98195, USA*



(Received 7 February 2020; revised manuscript received 3 May 2020; accepted 15 May 2020; published 3 June 2020)

First-principles, real-time-cumulant, and Bethe-Salpeter-equation calculations fully capture the detailed satellite structure that occurs in response to the sudden creation of the core hole in both photoemission and x-ray absorption spectra of the transition-metal compounds SrTiO₃ and rutile TiO₂. Analysis of the excited-state, real-space charge-density fluctuations betrays the physical nature of these many electron excitations that are shown to reflect the materials' solid-state electronic structure and chemical bonding. This first-principles development of the cumulant-based core hole spectral function is generally applicable to other systems and should become a standard tool for all similar spectroscopic analysis going beyond the quasiparticle physics of the photoelectric effect.

DOI: [10.1103/PhysRevB.101.245119](https://doi.org/10.1103/PhysRevB.101.245119)

I. INTRODUCTION

Satellites in core-level spectroscopies directly probe many-body interactions and electron correlation in atoms, molecules, and solids. They show up as features in x-ray-photoemission spectra at higher binding energies than the main or quasiparticle peak and correspond to valence excitations produced by the sudden creation of the core hole [1,2]. Consequently, they can reveal many details about a material's ground and excited-state electronic structures in addition to its response properties going beyond quasiparticle physics. While satellites in atomic and small molecular systems have been interpreted within the sudden and Hartree-Fock approximations [3], the precise nature of satellites in solid-state systems has remained a mystery, necessitating theoretical approaches that go further than the quasiparticle approximation of the photoelectric effect [4].

We demonstrate that these many electron excitations are accurately captured for x-ray photoelectron (XPS) and x-ray absorption (XAS) spectroscopy of the transition-metal compounds SrTiO₃ and rutile TiO₂ by a first-principles approach that combines Bethe-Salpeter-equation (BSE) and real-time-cumulant spectral function calculations to account for core hole dynamics and screening. This real-time, real-space approach has advantages over traditional frequency-based formalisms because it follows the time evolution of the many-body system and hence the excited-state electron-density fluctuations that embody the physical nature of the satellites, in addition to their underlying electronic structures.

II. EXPERIMENTAL DETAILS

Experiments were performed at the NIST beamlines SST-1 and SST-2 of the National Synchrotron Light Source II, Brookhaven National Laboratory. Commercially obtained [001] face polished SrTiO₃ and rutile TiO₂ single crystals were introduced into the vacuum chamber following sonication in acetone. XPS spectra were collected with photon energy 6000 eV using the high-resolution Si(333) reflection from a specially designed Si(111) double-crystal monochromator and a hemispherical electron analyzer with its acceptance cone oriented parallel to the x-ray electric-field polarization vector of the incident beam (SST-2). XAS spectra were collected by total electron yield as a function of sample geometry and incident flux. The Si(220) reflection of the double-crystal monochromator was used for the Ti *K*-edge measurements (SST-2), while the high-resolution 1200 lines/mm grating of a variable line spacing plane grating monochromator was used for the Ti *L*_{2,3}-edge measurements (SST-1). Details of the beamlines, vacuum systems, and experimental procedures are given elsewhere [5–8].

III. RESULTS AND DISCUSSION

Figure 1(a) compares the Ti 1*s* and Ti 2*p* XPS for single-crystal SrTiO₃, and Fig. 1(b) compares the Ti 1*s* and Ti 2*p* XPS for single-crystal rutile TiO₂. Common to each spectrum, besides to the zero-loss peak, is a high-energy satellite near 14-eV loss that has been the subject of numerous studies [9–14]; it peaks at 14-eV loss in SrTiO₃ and 13.5-eV

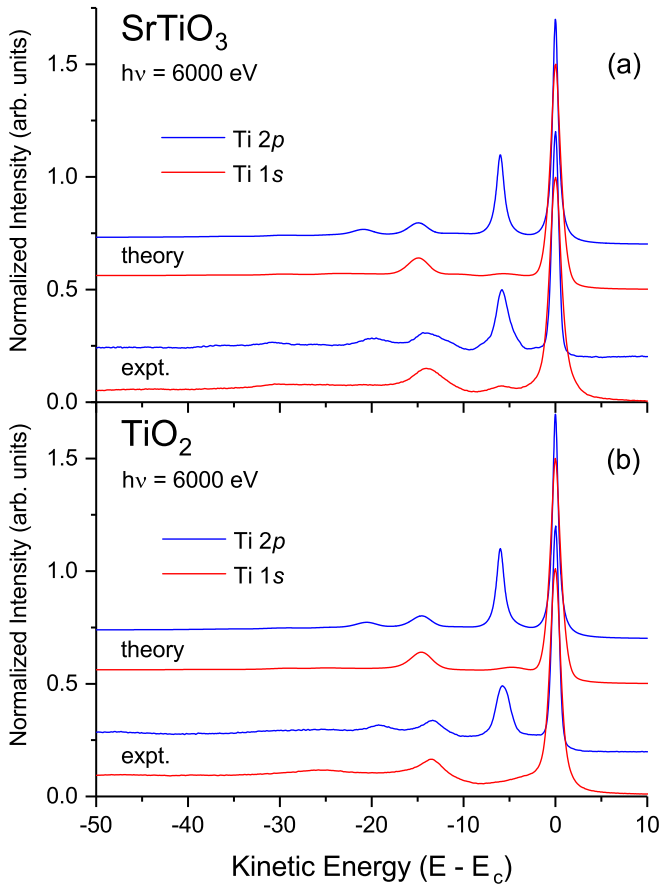


FIG. 1. (a) Calculated Ti 1s and Ti 2p XPS spectra for SrTiO₃ and experiment. (b) Calculated Ti 1s and Ti 2p XPS spectra for TiO₂ and experiment. The spectra have been normalized to unit peak height and offset for clarity.

loss in TiO₂. The Ti 1s spectra further reveal a low-energy, less intense structure near 6-eV loss [7,15,16]. The 5.6-eV spin-orbit splitting of the Ti 2p core level obfuscated this low-energy satellite prior to Ref. [7], as is evident from Figs. 1(a) and 1(b).

Differences between the Ti 1s XPS of the two materials are noteworthy. The low-energy satellite is not resolved in the TiO₂ spectrum; rather, it appears to merge into the low-energy tail of the Ti 1s core line. Also evident is additional intensity on the high-kinetic, low-binding-energy side of the 14-eV satellite in SrTiO₃ (near 11-eV loss), while in TiO₂ the 14-eV satellite appears symmetrical. Likewise, the Ti 2p core lines reflect similar differences.

Figure 2(a) shows the Ti K-edge XAS for SrTiO₃, and Fig. 2(b) shows the Ti K-edge XAS for rutile TiO₂. Common are a series of pre-edge features that are typically sported by such compounds; they have also been the subject of numerous studies [17–25]. Similarly, Figures 3(a) and 3(b) show the Ti L_{2,3}-edge XAS for each.

For the K edge, the dominant peaks occurring near 4985 eV are Ti 1s → 4p dipole transitions. The two lowest-energy peaks below the main edge are quadrupole transitions of the Ti 1s electron to the Ti 3d t_{2g} and Ti 3d e_g crystal-field split states of O_h symmetry [17–24]. (The Ti 1s → 3d t_{2g} transition occurs near 4969 eV, and the Ti 1s → 3d e_g transition occurs

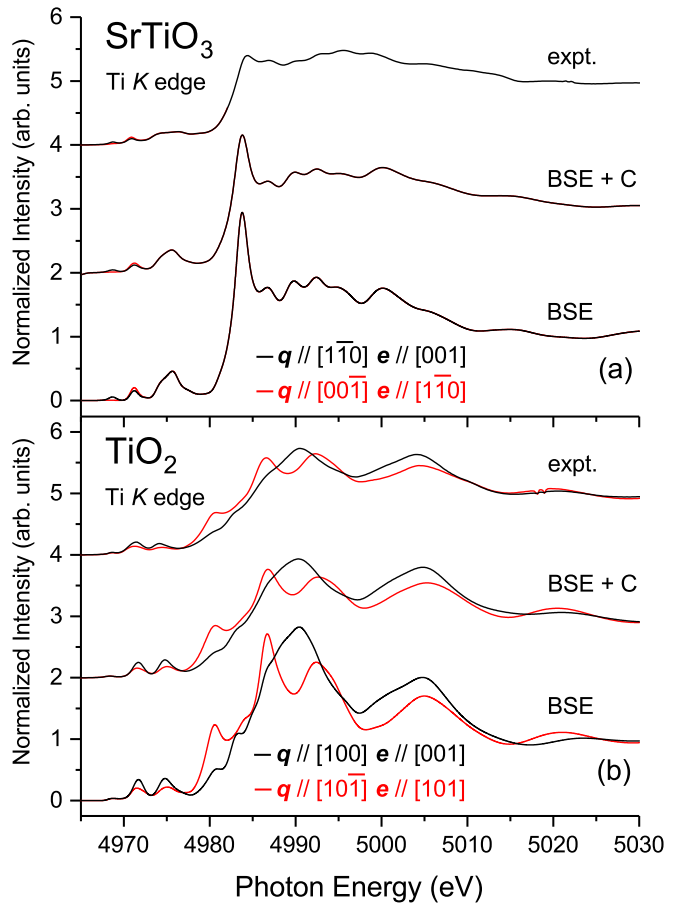


FIG. 2. (a) Calculated Ti 1s (K-edge) XAS spectra for SrTiO₃ and experiment. (b) Calculated Ti 1s (K-edge) XAS spectra for TiO₂ and experiment. Bottom: BSE theory. Middle: BSE + cumulant (C). Top: Experiment. The spectra have been normalized to unit step height and offset for clarity.

near 4971 eV.) The third low-energy feature occurring near 4975 eV arises from dipole transitions of the Ti 1s electron to the Ti 3d orbitals on next nearest neighbor (NNN) Ti atoms that result from local Ti 4p–O 2p–NNN Ti 3d mediated hybridization (i.e., “band-structure effects”). Such features are naturally modeled if one begins with a full band-structure treatment of Bloch states in the ground state, and are less directly accessible to cluster-based approaches. The fact that these transitions are dipole allowed and contribute such small intensity to the XAS emphasizes that most of their character originates from the neighboring metal-ion 3d states rather than from the central absorbing Ti atom. Also note that this peak is much wider in SrTiO₃ than in TiO₂, a band-structure effect that we address later.

For the L_{2,3} edge, the peaks below the first intense Ti 2p → 3d dipole transition are exchange and multiplet splitting that arise from the angular momentum coupling of the Ti 2p core hole with the photoexcited electron in the Ti 3d level [25]. (The Ti 2p_{3/2} → 3d t_{2g} transition occurs near 457.5 eV, and the Ti 2p_{3/2} → 3d e_g transition occurs near 460 eV.) Such features are not observed at the Ti K edge because of the much smaller overlap of the Ti 1s and Ti 3d orbitals and the simpler nature of the K shell. Both the 2.2-eV crystal-field

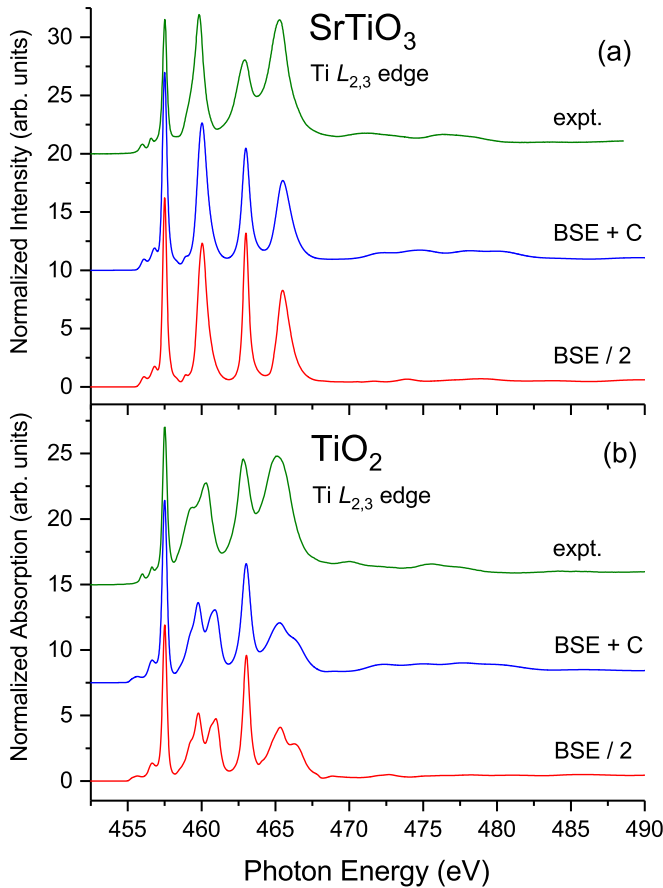


FIG. 3. (a) Calculated Ti $2p$ ($L_{2,3}$ -edge) XAS spectra for SrTiO₃ and experiment. (b) Calculated Ti $2p$ ($L_{2,3}$ -edge) XAS spectra for TiO₂ and experiment. Bottom: BSE theory. Middle: BSE + cumulant (C). Top: Experiment. The spectra have been normalized to unit step height and offset for clarity. The $L_{2,3}$ -edge BSE results have been divided by an additional factor of 2 as indicated.

splitting of the Ti $3d$ states and the 5.6-eV spin-orbit splitting of the Ti $2p$ core level are evident in the $L_{2,3}$ -edge data, and these dominant features are followed by their satellite losses that occur approximately 14 eV above each transition [13,26]. Note that the low-energy satellite is again obscured in the XAS by the spin-orbit splitting of the Ti $2p$ level, although it does introduce an asymmetry to the spin-orbit split $2p_{1/2}$ or higher-energy L_2 features in both the XPS and XAS of SrTiO₃. Beyond the foregoing discussion, there are also quadrupolar Coster-Kronig effects that further broaden the L_2 features and E - e pseudo-Jahn-Teller effects that further broaden the e_g -derived features [27].

Theoretically, apart from slowly varying matrix-element factors, XPS is directly related to the spectral function $A_c(\omega) = -(1/\pi)\text{Im}G_c(\omega)$ associated with the core hole Green's function $G_c(\omega)$. Here $G_c(\omega)$ is calculated via a real-time, time-dependent density-functional-theory (RT-TDDFT) cumulant approach as described previously [28]. Within this approximation, the core hole Green's function in the time domain is represented as an exponential $G_c(t) = -i\exp[i\varepsilon_c t + C(t)]$, where ε_c is the core-level binding energy associated with the main peak in XPS, and $C(t)$ is the cumulant. The cumulant in turn is given by $C(t) =$

$\int d\omega \frac{\beta(\omega)}{\omega^2} [e^{i\omega t} - i\omega t - 1]$, where $\frac{\beta(\omega)}{\omega} = \text{Re} \mathcal{F}[\Delta(t)]$ is the excitation spectrum, which has peaks corresponding to those in the loss function, and accounts for the many-body excitations. Finally, $\Delta(t) = \int d\mathbf{r} v_c(\mathbf{r})\delta\rho(\mathbf{r}, t)$ is found by integrating the density induced by the sudden appearance of the core hole potential. Since the cumulant is calculated in terms of the real-space, real-time density response to the sudden appearance of the core hole following photoexcitation, the method allows for real-space analysis of the excitations involved. In addition, the method in practice should be more efficient than frequency-space, plane-wave-based methods, which require a full calculation of the linear response function. Finally, the cumulant spectral function provides an improved description of many-body satellites seen in XPS over the often-used GW approximation of Hedin [29], with little if any added computational cost [30].

Figures 1(a) and 1(b) compare the experimental data to the theoretical spectra obtained from the RT-TDDFT calculations of the cumulant. In order to limit spurious interactions between core holes, the calculations were performed on a $3 \times 4 \times 4$, 240-atom supercell for SrTiO₃ and a $3 \times 3 \times 5$, 270-atom supercell for TiO₂. The full width at half maximum lifetime broadening of the satellites was set to 1.0 eV for all calculations, and the broadening of the main peak was set to 1.0 eV for the Ti $1s$ level, and 0.75 eV and 1.0 eV for the Ti $2p_{3/2}$ and Ti $2p_{1/2}$ levels for both SrTiO₃ and TiO₂, respectively. A Shirley background was also added to the calculations [31]. The quantitative agreement between the experimental data and the first-principles simulations is striking in general structure, position, and overall intensity relative to the primary core lines, albeit the theoretical calculations overestimate the binding energies of the satellites in both cases relative to their parent peaks.

We also calculated the Ti K -edge XAS and the Ti $L_{2,3}$ -edge XAS for SrTiO₃ and TiO₂ using the known crystal structures, the latter of which includes thermal vibrations at room temperature [32]. We used the BSE method as implemented in the OCEAN code [33], with theoretical broadening to simulate experimental resolution [34], electron-damping effects [35], and core hole-lifetime damping [36]. We also included exchange and multiplet effects in the Ti $L_{2,3}$ -edge calculations following the treatment of Ref. [22]. Although the BSE includes the excitonic Coulomb interaction between the core hole and the photoexcited electron, it is an incomplete theory of XAS because it does not account for many-body electron shake-up excitations. These excitations can be included in the BSE by convolution of the BSE spectrum $\mu'(\omega)$ with the theoretical photon-energy-dependent spectral function $A(\omega, \omega')$ *ex post facto* following Refs. [37–40]:

$$\mu(\omega) = \int d\omega' A(\omega, \omega') \mu'(\omega - \omega'). \quad (1)$$

In doing so, the cumulant correction supplants the self-energy damping of the electron as calculated in the GW approximation [35].

In general, $A(\omega, \omega')$ should include all excitations arising from interactions between valence electrons and the core hole (intrinsic) as well as interactions between valence electrons and the photoelectron (extrinsic) in addition to interference

terms between them [41]. In principle, such extrinsic and interference effects could be accounted for by an additional amplitude factor scaling the satellite strength, but these effects are of opposite sign and tend to cancel. Therefore, to maintain model independence, we simply replace $A(\omega, \omega')$ in Eq. (1) with the core hole spectral function $A_c(\omega)$. Equation (1) then becomes a standard convolution with $A_c(\omega)$ calculated using the RT-TDDFT cumulant approach.

For the K edge, convolution with the cumulant spectral function reduces the overstated BSE intensity of the excitonically enhanced Ti $1s \rightarrow 4p$ transition and redistributes it to the satellite binding energies consistent with the dipole sum rule for shake satellites [42]. Note as well the filling of the trough approximately 5 eV above the Ti $1s \rightarrow$ NNN Ti $3d$ feature in SrTiO₃. Similar changes are observed for TiO₂ as well; however, the onset of the p -wave maximum is still strongly exaggerated in SrTiO₃ albeit it is less strongly exaggerated in rutile TiO₂. As shown in Ref. [43], the leading absorption features can be strongly affected by modest changes in the core hole potential and its screening strength, becoming a larger problem with smaller dielectric constant (about 5 in SrTiO₃ and 6 in rutile TiO₂). We also note that the strength of the excitonically enhanced peak at the absorption maximum depends on the distribution of spectral weight near the peak itself, especially on its high-photon-energy side, making such calculations more problematic for SrTiO₃ than rutile.

For the L edge, convolution with the cumulant spectral function significantly reduces the overstated BSE intensity of the signature peaks: The relative intensity is now reduced by a full factor of 2, bringing the theoretical and experimental spectra into much better quantitative agreement; it also now adds distinct satellites to the XAS. This dramatic departure from the K -edge behavior arises from the much smaller baseline intensity or “edge jump” of the L edges that occurs on account of their intense dipole allowed Ti $2p \rightarrow 3d$ transitions, which dominate the spectra. (The Ti $1s \rightarrow 3d$ K -edge transitions are dipole forbidden.) Also observed are the different XAS-satellite structures for SrTiO₃ and TiO₂ that follow the main XAS-peak intensities in addition to the differences noted in the XPS.

The Ti $2p$ near-edge spectrum for SrTiO₃ and rutile TiO₂ have been calculated previously by a variety of methods [44,45]. These materials have also been studied by the BSE [46], but a poorer Ti pseudopotential was used there than in the present study [47]. It could still be true that the pseudopotential approximation is affecting the BSE results presented here, because of the Ti $3d$, $4s$, and $4p$ states in the solid. The pseudopotential is generated to ensure correct scattering properties at the Ti $3s$ and $3p$ energies, but it was iteratively generated in slightly different forms to enhance extended norm conservation and transferability [47]. There are also other differences in calculation method between these studies. Simple ranking of the quality of agreement with experiment would be too premature a criterion by which to assess the remaining approximations that are many in all theoretical works. The relative ordering of heights of the two peaks derived from a t_{2g} $3d$ electron and $J = 3/2$ core hole is incorrect in the present work and correct in the others, but the overall ratio of the heights is never far from unity in any case. What is more curious and unresolved is the relative spectral

weight and rounded shape of the feature derived from an e_g $3d$ electron and $J = 1/2$ core hole, which is poorly predicted by all theoretical works to date. Regardless, it should be noted that Ref. [44] applied an empirical *ad hoc* energy-dependent broadening to resemble the experiment, while the *ab initio* core hole spectral function developed here could instead be applied to those calculations that did not consider many electron (satellite) effects.

To determine the physical origin of the satellites, we also calculated the excited-state electron-density fluctuations $\Delta\rho(\mathbf{r}, \omega_{\text{sat}}) \equiv \text{Re } \mathcal{F} [\Delta\rho(\mathbf{r}, t)]$, where \mathcal{F} denotes the Fourier transform to frequency. These density fluctuations are shown in real-space at the charge-transfer satellite energies ω_{sat} for SrTiO₃ and TiO₂. Figure 4 (top) shows the fluctuations for SrTiO₃ calculated at frequencies corresponding to 14.8 and 6.0 eV, i.e., the dominant satellite binding energies in the theoretical XPS of SrTiO₃. (The 10.6-eV structure will be discussed below.) The high-energy satellite has the same shape as the Ti $3d e_g$ molecular orbitals of the [TiO₆]⁸⁻ cluster [48], confirming the early experimental assignment that this transition is ligand O $2p_\sigma$ to metal Ti $3d e_g$ charge transfer [7]. Note that the O s - p hybridization orients the charge density of the O $2p_\sigma$ orbitals towards the Ti atom [49]. The low-energy satellite, on the other hand, has a much more complicated density. Observed are transitions between the O $2p_\pi$ orbitals and the metal $3d t_{2g}$ orbitals [50]; however, unique to this transition is the charge that flows back to the O ligands. The π back bonding is a common occurrence in organic chemistry [51], but here it is observed in reverse through the e_g channel because of the π excitation and the much larger overlap of the O $2p_\sigma$ and Ti $3d e_g$ orbitals.

Figure 4 (bottom) shows the excited-state electron-density fluctuations for TiO₂ calculated at its theoretical satellite energies. The high-energy satellite again has the same shape as the e_g molecular orbitals of the [TiO₆]⁸⁻ cluster [48], and again it is much “cleaner” than the low-energy excitation. However, the low-energy satellite is now visibly more complex than the corresponding structure in SrTiO₃. We attribute this added complexity to the lower molecular point-group symmetry around the Ti atoms, O_h in SrTiO₃ versus D_{2h} in rutile TiO₂ [52], that splits the 6 Ti-O bonds into a two-bond apical and a four-bond equatorial set, each having its own bond length and local electronic structure as observed in Fig. 4. The energy of the low-energy satellite is also significantly reduced in TiO₂ relative to SrTiO₃, and this observation we reconcile with the smaller band gap of TiO₂ relative to SrTiO₃, which would naturally lower the energies of the nominally e_g and t_{2g} transitions [53,54].

To determine the origin of the intensity near 11-eV loss in SrTiO₃, we also calculated the density fluctuations corresponding to frequency 10.6 eV as shown in Fig. 4. The resulting fluctuations closely resemble the fluctuations of the 6-eV satellite, demonstrating that this satellite is also a t_{2g} excitation, but now involving a higher-energy region of the SrTiO₃ crystalline density of states. Interestingly, we also find that there is less distortion of the O $2p$ states at this higher energy. Given that the energy of the 11-eV loss is roughly double that of the low-energy satellite, it would be tempting to explain the 11-eV loss as a two 6-eV bosonlike excitation. However, this is not the case because the intensity at 11 eV

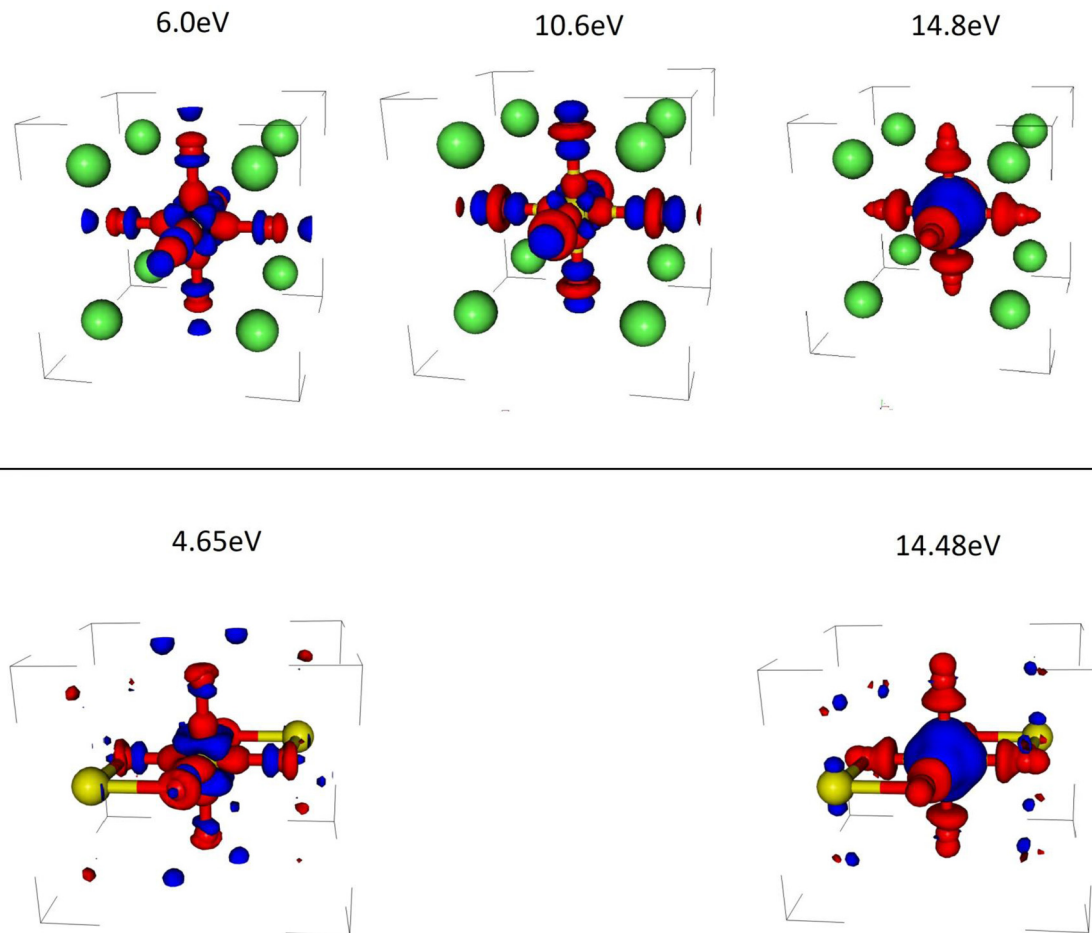


FIG. 4. Theoretical excited-state electron-density fluctuations $\Delta\rho(\mathbf{r}, \omega_{\text{sat}})$ calculated at frequencies corresponding to the theoretical satellite binding energies as indicated. Top: SrTiO₃. Bottom: TiO₂. Red indicates negative electron density and blue indicates positive electron density.

appears in the linear response to the core hole, which is related to the single-boson excitation spectrum.

The density fluctuations shown in Fig. 4 reflect monopole transitions between the occupied and unoccupied molecular orbitals of the crystal within the sudden approximation [2]. To establish their dependence on the materials' solid-state electronic structure, we calculated the product of coefficients between bonding and antibonding orbitals across the materials' band gap, as was done previously for MoS₂ [55]. The coefficients closely follow the crystalline partial densities of states; they also highlight the chemical bonding between the anions and cations of these ionic crystals, while excluding O nonbonding states that have been shown to dominate the top of the valence band [49]. The mixing coefficients are plotted in Fig. 5(a) for SrTiO₃ and in Fig. 5(b) for TiO₂. For SrTiO₃, the decomposition was made into pure e_g and t_{2g} contributions; however, D_{2h} symmetry lifts the triple degeneracy of the Ti 3d t_{2g} orbitals and the double degeneracy of the Ti 3d e_g orbitals that are hallmarks of O_h symmetry [56]. For TiO₂, the convention we use to denote a 3d state on a Ti site relates to whether the plane of its orbital lobes is *parallel* or *perpendicular* to the equatorial plane. As stated earlier, the equatorial plane contains the four equivalent Ti-O bonds, but we still use the terms e_g and t_{2g} to associate the orbitals with their ideal counterparts in an undistorted O₆ octahedron. We

choose the coordinate system such that the z axis is along the two apical Ti-O bonds, and the x and y axes are in the plane of the four equatorial Ti-O bonds, each being oriented along one of the two C_2 axes that also define that plane. This choice of coordinates renders the following enumeration of the metal 3d orbitals: $e_g(\perp) = 3d_{3z^2-r^2}$, $e_g(\parallel) = 3d_{x^2-y^2}$, $t_{2g}(\perp) = 3d_{xz}$ or $3d_{yz}$, and $t_{2g}(\parallel) = 3d_{xy}$. For simplicity, we also neglect s - d and d - g hybridization allowed by the Ti- D_{2h} site symmetry.

Several observations are noteworthy. First, the width of the unoccupied e_g states that are primarily of metal 3d character are significantly wider for SrTiO₃ than for TiO₂ accounting for the much broader Ti 4p-O 2p-NNN Ti 3d transition (i.e., the third peak in the Ti K-edge XAS) in SrTiO₃ versus TiO₂. This peak is dominated by Ti 3d e_g rather than Ti 3d t_{2g} transitions on account of the much larger overlaps found in σ versus π bonding; it closely follows the metal 3d e_g conduction-band density of states because of the diminished core hole potential on the neighboring metal sites [21]. The splitting of the TiO₂ e_g peaks in the unoccupied density of states also accounts for the splitting of the e_g contributions to the Ti L-edge XAS of TiO₂. Concerning the satellite structures, the additional width and splitting of the TiO₂ t_{2g} peaks both above and below the Fermi level account for the blurring of the low-energy satellite in the XPS spectra of TiO₂, as well as the absence of a second higher-energy t_{2g} feature

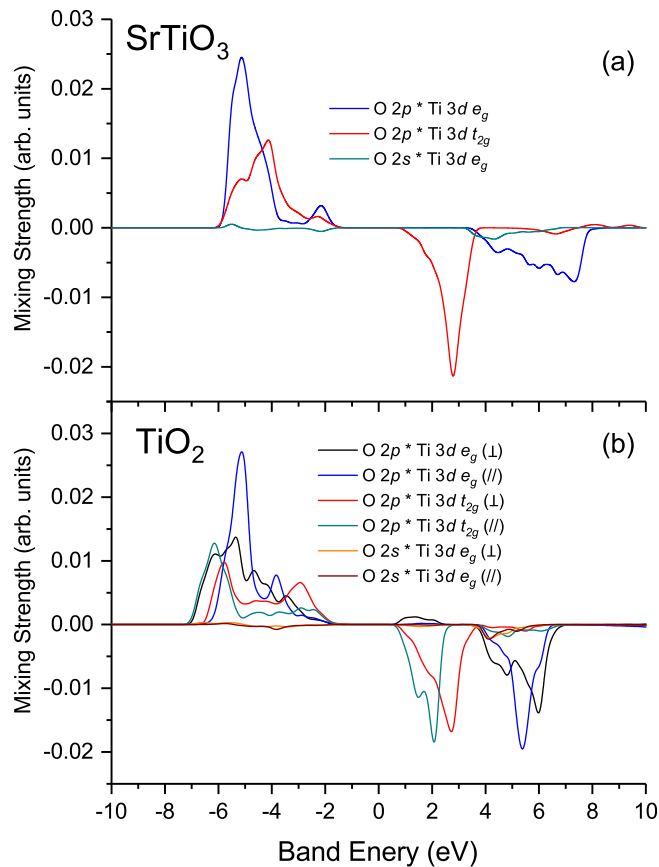


FIG. 5. Mixing strengths of the Ti $3d$ orbitals and neighboring O $2s$ and O $2p$ orbitals belonging to different representations of the group of the Ti site. (a) SrTiO₃. (b) TiO₂. For SrTiO₃, the decomposition was made into the pure e_g and t_{2g} contributions of O_h symmetry, whereas for rutile TiO₂, the D_{2h} molecular point-group symmetry around the Ti ion organizes the orbitals into four sets relative to the equatorial plane formed by the four equivalent Ti-O bonds (ignoring s - d and d - g mixing; see text).

in either theory or experiment. In addition, it is likely that the higher-energy t_{2g} satellite in the XPS of SrTiO₃ corresponds to higher-energy t_{2g} transitions that energetically lie completely within the unoccupied e_g density of states. The fact that there can be no bonding contribution between the O $2s$ orbitals and the metal $3d$ t_{2g} orbitals suggests that the asymmetry found in the low-energy charge-density fluctuations around the O atoms arises from Ti $3d$ -O $2p$ level repulsion from the central and neighboring Ti atoms rather than from O s - p hybridization. These effects appear to diminish at higher energy, consistent with the smaller density of metal charge observed. Strictly speaking, there can be no O s - p hybridization in SrTiO₃ because of the O- D_{4h} site symmetry, whereas there can always be core hole induced O s - p hybridization. However, the O $2s$ and $2p$ orbitals can mix with the Ti $3d$ e_g orbitals in all cases. All of this is consistent with the behavior of the charge-density fluctuations shown in Fig. 4.

To further explore the consequences of the reduced site symmetry of TiO₂, Fig. 6 shows an expanded energy view of the polarization dependence of the first Ti $2p \rightarrow 3d$ t_{2g} transition of the Ti $L_{2,3}$ edge. Observed is an approximate

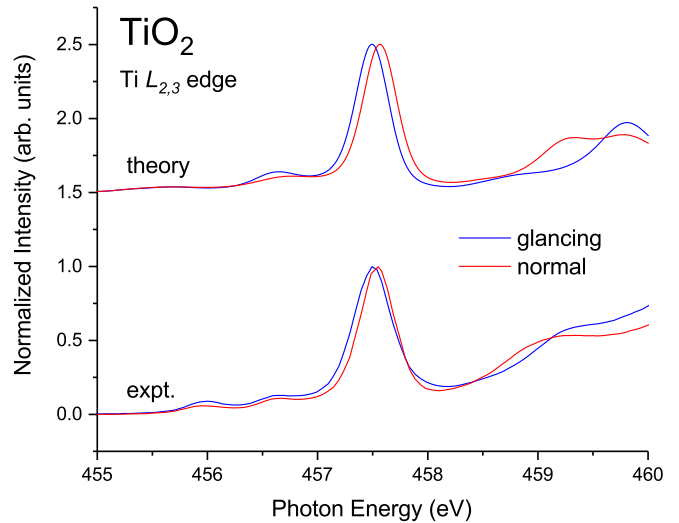


FIG. 6. Calculated Ti $2p$ ($L_{2,3}$ -edge) XAS spectra for TiO₂ and experiment. The spectra have been normalized to unit peak height and offset for clarity.

0.1-eV shift of the Ti $3d$ t_{2g} L_3 peak when the polarization vector is along the rutile c axis (glancing incidence) or perpendicular to it (normal incidence). This shift is consistent with the energy shifts of the t_{2g} peaks in the unoccupied density of states for TiO₂ displayed in Fig. 5; however, we note that it is counter to what would be predicted by simple crystal-field theory based on the longer apical versus the shorter equatorial Ti-O bond lengths [56] and the favorable sampling of the former at normal and the latter at glancing incidence.

IV. CONCLUSIONS

In conclusion, we have combined first-principles BSE calculations with the cumulant representation of the core hole Green's function within RT-TDDFT to account for multielectron charge-transfer effects in both the XPS and XAS of SrTiO₃ and rutile TiO₂; i.e., going beyond the GW quasiparticle approximation of the photoelectric effect. The predictive potential of the cumulant was demonstrated *a priori* by XPS and applied *a posteriori* to XAS. We analyzed the satellite structures by the theoretical real-space electron-density response to the sudden creation of the core hole and the materials' site-specific electronic structure and chemical bonding. Additional crystal-field splitting of the Ti $3d$ orbitals by the lower Ti-site symmetry of TiO₂ was also observed and reproduced theoretically. The first-principles developments presented here are generally applicable to other systems and should become a standard tool with application to all similar spectroscopic analysis.

ACKNOWLEDGMENTS

This work was performed at the National Synchrotron Light Source II, Brookhaven National Laboratory, beamlines SST-1 and SST-2 of the National Institute of Standards and Technology. Use of the National Synchrotron Light Source was supported by the U.S. Department of Energy,

Office of Basic Energy Sciences, under Contract No. DE-AC02-98CH10886. J.J.R. and J.J.K. acknowledge support

from DOE Office of Sciences BES Grant No. DE-FG02-97ER45623.

- [1] K. Siegbahn, C. Nordling, G. Johansson, J. Hedman, P. H. Hedén, K. Hamrin, U. Gelius, T. Bergmark, L. O. Werme, R. Manne, and Y. Baer, *ESCA Applied to Free Molecules* (North-Holland, Amsterdam, 1969).
- [2] T. A. Carlson, *Photoelectron and Auger Spectroscopy* (Plenum Press, New York, 1975).
- [3] T. Åberg, *Phys. Rev.* **156**, 35 (1967).
- [4] L. Hedin, in *Solid-State Photoemission and Related Methods: Theory and Experiment*, edited by W. Schattke and M. A. Van Hove (Wiley-VCH, Weinheim, 2003).
- [5] C. Weiland, A. K. Rumaiz, P. Lysaght, B. Karlin, J. C. Woicik, and D. A. Fischer, *J. Electron Spectrosc. Relat. Phenom.* **190**, 193 (2013).
- [6] C. Weiland, C. Jaye, N. F. Quackenbush, E. Gann, Z. Fu, J. P. Kirkland, B. A. Karlin, B. Ravel, J. C. Woicik, and D. A. Fischer, *Synchrotron Radiat. News* **31**, 23 (2018).
- [7] J. C. Woicik, C. Weiland, and A. K. Rumaiz, *Phys. Rev. B* **91**, 201412(R) (2015).
- [8] R. Reininger, J. C. Woicik, S. L. Hulbert, and D. A. Fischer, *Nucl. Instrum. Methods Phys. Res., Sect. A* **649**, 49 (2011).
- [9] I. Ikemoto, K. Ishii, H. Kuroda, and J. M. Thomas, *Chem. Phys. Lett.* **28**, 55 (1974).
- [10] K. S. Kim and N. Winograd, *Chem. Phys. Lett.* **31**, 312 (1975).
- [11] S. K. Sen, J. Riga, and J. Verbist, *Chem. Phys. Lett.* **39**, 560 (1976).
- [12] A. E. Bocquet, T. Mizokawa, K. Morikawa, A. Fujimori, S. R. Barman, K. Maiti, D. D. Sarma, Y. Tokura, and M. Onoda, *Phys. Rev. B* **53**, 1161 (1996).
- [13] K. Okada and A. Kotani, *J. Electron Spectrosc. Relat. Phenom.* **62**, 131 (1993).
- [14] R. Zimmermann, P. Steiner, R. Claessen, F. Reinert, S. Hüfner, P. Blaha, and P. Dufek, *J. Phys.: Condens. Matter* **11**, 1657 (1999).
- [15] B. Gobaut, P. Orgiani, A. Sambri, E. di Gennaro, C. Aruta, F. Borgatti, V. Lollobrigida, D. Céolin, J.-P. Rueff, R. Ciancio, C. Bigi, P. K. Das, J. Fujii, D. Krizmancic, P. Torelli, I. Vobornik, G. Rossi, F. M. Granozio, U. S. di Uccio, and G. Panaccione, *ACS Appl. Mater. Interfaces* **9**, 23099 (2017).
- [16] A. Regoutz, M. Mascheck, T. Wiell, S. K. Eriksson, C. Liljenberg, K. Tetzner, B. A. D. Williamson, D. O. Scanlon, and P. Palmgren, *Rev. Sci. Instrum.* **89**, 073105 (2018).
- [17] T. Uozumi, K. Okada, A. Kotani, O. Durmeyer, J. P. Kappler, E. Beaurepaire, and J. C. Parlebas, *Europhys. Lett.* **18**, 85 (1992).
- [18] R. V. Vedrinskii, V. L. Kraizman, A. A. Novakovich, Ph. V. Demekhin, and S. V. Urazhdin, *J. Phys.: Condens. Matter* **10**, 9561 (1998).
- [19] D. Cabaret, Y. Joly, H. Renevier, and R. Natoli, *J. Synchrotron Radiat.* **6**, 258 (1999).
- [20] J. Danger, P. Le Fevre, H. Magnan, D. Chandesris, S. Bourgeois, J. Jupille, T. Eickhoff, and W. Drube, *Phys. Rev. Lett.* **88**, 243001 (2002).
- [21] T. Yamamoto, T. Mizoguchi, and I. Tanaka, *Phys. Rev. B* **71**, 245113 (2005).
- [22] J. C. Woicik, E. L. Shirley, C. S. Hellberg, K. E. Andersen, S. Sambasivan, D. A. Fischer, B. D. Chapman, E. A. Stern, P. Ryan, D. L. Ederer, and H. Li, *Phys. Rev. B* **75**, 140103(R) (2007).
- [23] Z. Y. Wu, D. C. Xian, T. D. Hu, Y. N. Xie, Y. Tao, C. R. Natoli, E. Paris, and A. Marcelli, *Phys. Rev. B* **70**, 033104 (2004).
- [24] T. Yamamoto, *X-Ray Spectrom.* **37**, 572 (2008).
- [25] F. M. F. de Groot, J. C. Fuggle, B. T. Thole, and G. A. Sawatzky, *Phys. Rev. B* **41**, 928 (1990).
- [26] G. Van Der Laan, C. S. Mythen, and H. A. Padmore, *Europhys. Lett.* **11**, 67 (1990); G. van der Laan, *Phys. Rev. B* **41**, 12366(R) (1990).
- [27] K. Gilmore and E. L. Shirley, *J. Phys.: Condens. Matter* **22**, 315901 (2010).
- [28] J. J. Kas, F. D. Vila, J. J. Rehr, and S. A. Chambers, *Phys. Rev. B* **91**, 121112(R) (2015).
- [29] L. Hedin, *Phys. Rev.* **139**, A796 (1965).
- [30] J. S. Zhou, J. J. Kas, L. Sponza, I. Reshetnyak, M. Guzzo, C. Giorgetti, M. Gatti, F. Sottile, J. J. Rehr, and L. Reining, *J. Chem. Phys.* **143**, 184109 (2015).
- [31] D. A. Shirley, *Phys. Rev. B* **5**, 4709 (1972).
- [32] E. Cockayne, E. L. Shirley, B. Ravel, and J. C. Woicik, *Phys. Rev. B* **98**, 014111 (2018).
- [33] K. Gilmore, J. Vinson, E. L. Shirley, D. Prendergast, C. D. Pemmaraju, J. J. Kas, F. D. Vila, and J. J. Rehr, *Comput. Phys. Commun.* **197**, 109 (2015).
- [34] The experimental-Gaussian resolution of the double-crystal Si(220) monochromator is estimated to be 0.33 eV at the Ti K edge.
- [35] E. L. Shirley, *Radiat. Phys. Chem.* **167**, 108165 (2020).
- [36] M. O. Krause and J. H. Oliver, *J. Phys. Chem. Ref. Data* **8**, 329 (1979), The lifetime-Lorentzian width is estimated to be 0.94 eV for the Ti 1s core, and 0.22 and 0.24 eV for the $2p_{3/2}$ and $2p_{1/2}$ cores, respectively.
- [37] P. Nozières and C. T. de Dominicis, *Phys. Rev.* **178**, 1097 (1969).
- [38] L. Campbell, L. Hedin, J. J. Rehr, and W. Bardyszewski, *Phys. Rev. B* **65**, 064107 (2002).
- [39] M. Calandra, J. P. Rueff, C. Gougoussis, D. Céolin, M. Gorgoi, S. Benedetti, P. Torelli, A. Shukla, D. Chandesris, and C. Brouder, *Phys. Rev. B* **86**, 165102 (2012).
- [40] E. Klevak, J. J. Kas, and J. J. Rehr, *Phys. Rev. B* **89**, 085123 (2014).
- [41] L. Hedin, *J. Phys.: Condens. Matter* **11**, R489 (1999).
- [42] E. A. Stern, B. A. Bunker, and S. M. Heald, *Phys. Rev. B* **21**, 5521 (1980).
- [43] E. L. Shirley, J. A. Soininen, and J. Rehr, *Phys. Scr.* **T115**, 31 (2005).
- [44] P. Krüger, *Phys. Rev. B* **81**, 125121 (2010).
- [45] R. Laskowski and P. Blaha, *Phys. Rev. B* **82**, 205104 (2010).
- [46] E. L. Shirley, *J. Electron Spectrosc. Relat. Phenom.* **144-147**, 1187 (2005).
- [47] E. L. Shirley, D. C. Allan, R. M. Martin, and J. D. Joannopoulos, *Phys. Rev. B* **40**, 3652 (1989).

- [48] M. Karplus and R. N. Porter, *Atoms and Molecules* (W. A. Benjamin, New York, 1970), Chap. 6.4.
- [49] J. C. Woicik, E. J. Nelson, L. Kronik, M. Jain, J. R. Chelikowsky, D. Heskett, L. E. Berman, and G. S. Herman, *Phys. Rev. Lett.* **89**, 077401 (2002).
- [50] The O $2p_\pi$ orbitals appear as red annuli because the sum of the p_x and p_y probability densities has no azimuthal dependence and is zero along the z direction. Similarly, although the Ti d_{xy} , d_{yz} , and d_{zx} orbitals point between the metal-ligand axes, the sum of their squares points towards the corners of the SrTiO₃ cube unit cell and not towards its edges.
- [51] A. Diefenbach, F. M. Bickelhaupt, and G. Frenking, *J. Am. Chem. Soc.* **122**, 6449 (2000).
- [52] K. M. Glassford and J. R. Chelikowsky, *Phys. Rev. B* **46**, 1284 (1992).
- [53] M. Landmann, E. Rauls, and W. G. Schmidt, *J. Phys.: Condens. Matter* **24**, 195503 (2012).
- [54] L. Sponza, V. Véniard, F. Sottile, C. Giorgetti, and L. Reining, *Phys. Rev. B* **87**, 235102 (2013).
- [55] J. C. Woicik, C. Weiland, A. K. Rumaiz, M. Brumbach, N. F. Quackenbush, J. M. Ablett, and E. L. Shirley, *Phys. Rev. B* **98**, 115149 (2018).
- [56] F. A. Cotton, *Chemical Applications of Group Theory*, 2nd ed. (Wiley-Interscience, New York, 1971).